

# Co-Optimization of Mission Profile and Aircraft Design for Cost-Effective Climate Impact Mitigation

Lambrecht, Nicholas R.; Varriale, Carmine; Proesmans, Pieter-Jan

DOI

10.13009/EUCASS2025-099

Publication date

**Document Version**Final published version

Citation (APA)

Lambrecht, N. R., Varriale, C., & Proesmans, P.-J. (2025). *Co-Optimization of Mission Profile and Aircraft Design for Cost-Effective Climate Impact Mitigation*. Paper presented at 11th European conference for aeronautics and space sciences, Rome, Italy. https://doi.org/10.13009/EUCASS2025-099

Important note

To cite this publication, please use the final published version (if applicable). Please check the document version above.

Copyright

Other than for strictly personal use, it is not permitted to download, forward or distribute the text or part of it, without the consent of the author(s) and/or copyright holder(s), unless the work is under an open content license such as Creative Commons.

Takedown policy

Please contact us and provide details if you believe this document breaches copyrights. We will remove access to the work immediately and investigate your claim.

# Co-Optimization of Mission Profile and Aircraft Design for Cost-Effective Climate Impact Mitigation

Nicholas Lambrecht, Carmine Varriale<sup>†</sup> and Pieter-Jan Proesmans

Delft University of Technology

Delft, The Netherlands

nrlambrecht@gmail.com · C.Varriale@tudelft.nl · P.Proesmans@tudelft.nl

†Corresponding author

#### **Abstract**

The trade-off between Direct Operating Costs (DOC) and the 100-year global Average Temperature Response (ATR $_{100}$ ) is investigated through simultaneous mission profile and design optimization of a narrow-body aircraft. First, a 4000 km 2D mission profile is optimized using Optimal Control Theory, for a fixed baseline aircraft design and varying the relative weight of DOC and ATR $_{100}$  in the objective function. The resulting trade-off curve shows that a 49% reduction in ATR $_{100}$  can be obtained with only a 0.42% increase in DOC. Next, the wing plan form is simultaneously optimized with the mission profile in a Multi-disciplinary Design Optimization framework. The updated trade-off curve improves overall, and shows a 56% reduction in ATR $_{100}$  corresponding to a 0.32% increase in DOC. We conclude that contrail avoidance is a cost-effective method of minimizing the climate effects of aviation.

# 1. Introduction

As the climate impact of aviation becomes better understood, new avenues in aircraft design and operations are being explored to mitigate global warming. Two thirds of the Effective Radiative Forcing (ERF) caused by aviation is attributed to non-CO<sub>2</sub> effects, mainly due to contrails and nitrogen oxides.<sup>1</sup> Contrails and contrail-induced cirrus account for more than half of the total aviation-induced ERF, and require particular attention to reduce their impact. Contrails form only in atmospheric regions where the humidity is high enough to allow condensation of engine exhaust gases, and persists in Ice-Supersaturated Regions (ISSRs) of the atmosphere.<sup>2</sup> These are regions where ice particles will not readily dissolve and often appear at typical cruise altitudes of commercial aircraft. Therefore, to avoid contrail formation and/or reduce their persistence, typical mission profiles may need to change. Because cruise altitude and Mach number are critical factors which drive the design of high-subsonic commercial transport aircraft, it is important to reconsider optimal aircraft designs together with their corresponding mission profile.

This paper proposes co-optimization of mission profiles and aircraft designs as an effective way of demonstrating the potential for climate impact reduction. It presents a methodology based on Multidisciplinary Design Optimization (MDO) and Optimal Control Theory (OCT), which results in optimal aircraft designs flying globally optimal mission profiles in a 2-dimensional vertical plane. The objective of the optimization is a weighted sum of two metrics, one to estimate climate impact, expressed in terms of the Average Temperature Response (ATR), and one for Direct Operating Costs (DOC). The relative weight of the two sub-objectives is varied to create a spectrum of solutions between the fully climate-optimal and fully cost-optimal ones, hence drawing a trade-off curve.

Climate impact is measured in terms of the Average Temperature Response over a 100-year period ATR<sub>100</sub>.<sup>3</sup> The ATR estimates the global mean near-surface temperature change, considering sustained emissions from an aircraft fleet.<sup>4</sup> Gaseous emissions of carbon dioxide (CO<sub>2</sub>), nitrogen oxides (NO<sub>x</sub>), sulphates (SO<sub>4</sub>), soot, and water vapour (H<sub>2</sub>O) are considered, as well as the effects of contrails. DOC are composed of fuel and time-dependent costs associated with a flight, where the latter includes crew salaries and time-dependent maintenance costs. Aircraft designs and mission profiles are traditionally optimized to minimize DOC.

The aircraft design is optimized by manipulating its wing plan form, which is parameterized in terms of aspect ratio, wing sweep, and wing loading, as these are high-level variables closely linked to the cruise altitude and cruise Mach number. The optimal mission profile is calculated by systematically adjusting the position of trajectory nodes while complying with the equations of motion for a point-mass with variable weight. The investigation focuses on medium-range flights (4000 km) covered by narrow-body aircraft. Landing and Take-off Operations (LTO) are ex-

cluded from the mission profile, for which the start and end points are fixed at 1000 m altitude. The methodology is implemented using the open-source Dymos library.<sup>5</sup>

The paper builds on the work by Proesmans and Vos,<sup>6</sup> who optimized an aircraft design for minimum climate impact while assuming a climb-cruise trajectory at constant Mach number. Although the initial cruise altitude and Mach number were design variables, the mission profile shape was fixed. They showed that the climate impact, in terms of ATR<sub>100</sub>, could be reduced by 50% for a 1.8% increase in DOC. Using a different optimization approach, Lührs et al.<sup>7</sup> achieved similar results. They showed that ATR could be reduced by 45% for a 2% rise in operating costs when using 3-dimensional flight path optimization for a wide-body aircraft. However, the study did not consider updates in the aircraft design. In this work, a constrained optimization setup can freely determine the entire flightpath, considering the start and end points mentioned above. For this reason, it is expected that the aircraft will spend more time at a cost-optimal cruise condition, and divert below or above climate-sensitive regions only when necessary.

# 2. Methodology

For the general optimization problem presented in this paper, aircraft design and mission profile optimizations are coupled in a single monolithic MDO problem formulation. The mathematical structure of the problem follows that suggested by Kaneko and Martins,<sup>8</sup> which is reported in Equation 1 and explained in the following paragraphs.

Minimise: 
$$J(t, \xi(t), u(t), p)$$
 (1a)  
by varying:  $\xi_{LB} \leq \xi(t) \leq \xi_{UB}$   
 $u_{LB} \leq u(t) \leq u_{UB}$  (1b)  
 $p_{LB} \leq p \leq p_{UB}$   
subject to:  $\dot{\xi} = f(\xi(t), u(t), t, p)$   
 $g_{\text{path}}(\xi(t), u(t), t, p) \leq 0$   
 $g_{\text{boundary}}(t_0, t_f, \xi(t_0), \xi(t_f)) \leq 0$ 

Equation 1a represents the objective function J as a generic function of the states  $\xi$ , controls u and design parameters p of the dynamic system whose geometry and evolution need to be optimized. Aircraft design parameters are statically parameterized, which means they are optimized alongside the trajectory but remain time-invariant. Equations 1b bound the latter sets of variables between prescribed, fixed limits. Equations 1c describe the functional constraints acting on the system. The first set describes the dynamics of the system and is therefore written in terms of the rate of change of the states  $\dot{\xi}$ . Path constraints  $g_{\text{path}}$  and boundary constraints  $g_{\text{boundary}}$  limit the evolution of the system along the flight path and at its initial and final instants, respectively. They apply directly to state and control variables, but indirectly affect design parameters as well. Static constraints  $g_{\text{static}}$  apply only to the design parameter.

The objective function is expressed as a weighted sum of  $ATR_{100}$  and DOC, as reported in Equation 2.

$$J = \psi \frac{\text{DOC}}{\text{DOC}_{\text{ref}}} + (1 - \psi) \frac{\text{ATR}_{100}}{\text{ATR}_{100 \text{ ref}}}, \quad 0 \le \psi \le 1, \quad \text{DOC}, \text{ATR}_{100} = f(t, \xi(t), \mathbf{u}(t), \mathbf{p})$$
 (2)

The cost weighting  $\psi$  determines the priority of DOC against the ATR<sub>100</sub> in the optimization, as formulated by Lührs et al.<sup>7</sup> A cost-optimal solution is obtained with  $\psi = 1$ , while a "climate-optimal" solution is obtained with  $\psi = 0$ . DOC<sub>ref</sub> and ATR<sub>100,ref</sub> are the values associated with a cost-optimal trajectory and baseline aircraft design. NO<sub>x</sub> impacts are not included in the ATR<sub>100</sub> objective, but are calculated *a posteriori* in the assessment of the climate impact of a resulting mission profile and aircraft configuration.

The states  $\xi$ , controls u, and design variables p are specified in Table 1, together with their upper bound, lower bound, and reference value for normalization. The angle of attack  $\alpha$  and turbine entry temperature  $T_{14}$  have been selected as variables to control the aircraft dynamic evolution in light of the chosen form of the aero-propulsive model, presented later in Section 3. Table 2 specifies the path and boundary constraints. The boundary constraints ensure comparable results by fixing the mission range, and the altitude and airspeed at the initial and final instants. Restrictions on the final acceleration and flight path angle enforce desired behaviour for a descent phase at constant speed.

The dynamic evolution of the aircraft is discretized over a time-domain mesh using a Legendre-Gauss-Radau (LGR) pseudospectral collocation method, based on strong literature support for its appropriateness to mission profile optimization problems.<sup>8–11</sup> The solution is explicitly represented and optimized at a set of 12 nodes in the time domain. Over each interval between nodes, the evolution of the states is approximated by fourth-order LGR interpolating polynomials.

Type	Name	Symbol	Reference	Lower bound	Upper bound	Unit
Controls	Angle of attack	α	1	-1	8	deg
	Turbine entry temp.	$T_{t4}$	1000	_	1700	K
States	Altitude	h	500	500	13 500	m
	Aircraft mass	m	$30 \times 10^{3}$	$m_{\rm OE} + m_{\rm pay}$	MTOM	kg
	Fuel mass used	$m_{ m f}$	$1 \times 10^{3}$	0	_	kg
	Horizontal distance	r	100	0	_	km
	Airspeed	V	100	150	280	${\rm ms^{-1}}$
	Flight path angle	γ	2	-3	3	deg
	ATR	$ATR_{100}$	$8 \times 10^{-4a}$	_	_	K
Indep.	Time	t	8000	0	$3 \times 10^{4}$	S

Table 1: Flight state and control variables

<sup>&</sup>lt;sup>a</sup>Determined on the basis of an expected total ATR of 10 mK to 20 mK

Name	Symbol	Lower path	Upper path	Initial condition	Final condition	Unit
Altitude	h	_	_	1000	1000	m
Mach number	M	_	0.9	_	_	_
Horizontal distance	r	_	_	0	4000	km
Thrust	T	0.0	_			N
Airspeed	V	_	_	150	150	${\rm m}{\rm s}^{-1}$
Airspeed rate	$\dot{V}$	-0.15	0.15		0	${ m m\ s^{-2}}$
Flight path angle	γ	_	_		$\geq -3.0$	deg
Flight path angular rate	ν̈́	-0.01	0.01	_		deg s⁻

Table 2: Mission path and boundary constraints

The aircraft configuration parameters are categorized as: design variables, for the optimizer to manipulate, fixed parameters, assigned on the basis of assumptions, and dependent variables, calculated as functions of the previous ones. They are specified in Tables 3a, 3b, and 3c, respectively. The wing surface area and wing span are determined from the wing loading, aspect ratio, and design Maximum Take-off Mass (MTOM). The approach wing loading  $W/S_{\rm app}$  is derived from the design Maximum Landing Mass (MLM). Maximum lift coefficients during cruise and approach are estimated from the quarter-chord sweep  $\Lambda_{\rm qc}$  according to Equation 3. These simple relations are based on experimental lift polar data from commercial aircraft studied by Obert. <sup>12</sup>

$$C_{L_{\text{buff}}} = 0.86 \cos \Lambda_{\text{qc}}$$
  $C_{L_{\text{max, app}}} = 2.9 \cos \Lambda_{\text{qc}}$  (3)

As for design parameter constraints, the maximum wing span is limited to  $b_{\text{max}} = 36 \,\text{m}$  in order to adhere to the ICAO Aerodrome Reference Code C, the maximum cruise lift coefficient is limited to avoid buffet ( $C_{L_{\text{buff}}}$  in Equation 3), and the maximum wing loading in approach conditions is also limited in relation to the maximum lift coefficient achievable in those conditions. These constraints are summarized in Equation 4.

$$b \le b_{\text{max}}$$
  $C_L \le \frac{C_{L_{\text{buff}}}}{1.3}$   $W/S_{\text{app}} \le \frac{1}{2}\rho_0 \left(\frac{V_{\text{app}}}{1.23}\right)^2 C_{L_{\text{max}}}$  (4)

The approach and wing span constraints are static design constraints. Approach conditions assume standard sea-level air density  $\rho_0 = 1.225 \,\mathrm{kg} \,\mathrm{m}^{-3}$  and an approach speed of  $V_{\rm app}$  of  $70 \,\mathrm{m} \,\mathrm{s}^{-1}$ . Since the buffet constraint is relevant to every point along the mission profile, it is applied as a path constraint, and the lift coefficient  $C_L$  is taken at each node in the mission profile. Because of its effect on both the buffet and maximum lift coefficients, the sweep angle  $\Lambda$  creates a direct coupling between aircraft design, landing performance (calculated with the simple equilibrium equation above), and cruise performance, calculated via dynamic simulation within the OCP.

The eXtended Design Structure Matrix (XDSM)<sup>13</sup> representing the MDO workflow that implements the described optmization problem is shown in Figure 1. Each of the models is described in more detail in the following section.

Table 3: Aircraft configuration parameters

#### (a) Design variables

Name	Symbol	Baseline	Lower bound	Upper bound	Unit
Wing aspect ratio	A	10.45	6	13	_
Wing loading	W/S	5881	4000	8000	${ m N}{ m m}^{-2}$
Wing quarter-chord sweep angle	$\Lambda_{ m qc}$	25.0	0	40	deg

# (b) Fixed parameters

# (c) Dependent variables

Name	Symbol	Baseline
Max. Take-Off Mass	MTOM	73 500 kg
Max. Landing Mass	MLM	$64500\mathrm{kg}$
Operating Empty Mass	$m_{ m OE}$	$42400\mathrm{kg}$
Reserve Fuel Mass	$m_{\rm res}$	$4300\mathrm{kg}$
Payload Mass	$m_{\rm pay}$	Case dependent

Name	Symbol	Baseline
Wing area	S	$122.6\mathrm{m}^2$
Wing span	b	35.8 m
Approach wing loading	$W/S_{\rm app}$	$5161  N  m^{-2}$
Buffet lift coeff.	$C_{L_{ m buff}}$	0.779
Max. lift coeff.	$C_{L_{ m max}}$	2.54

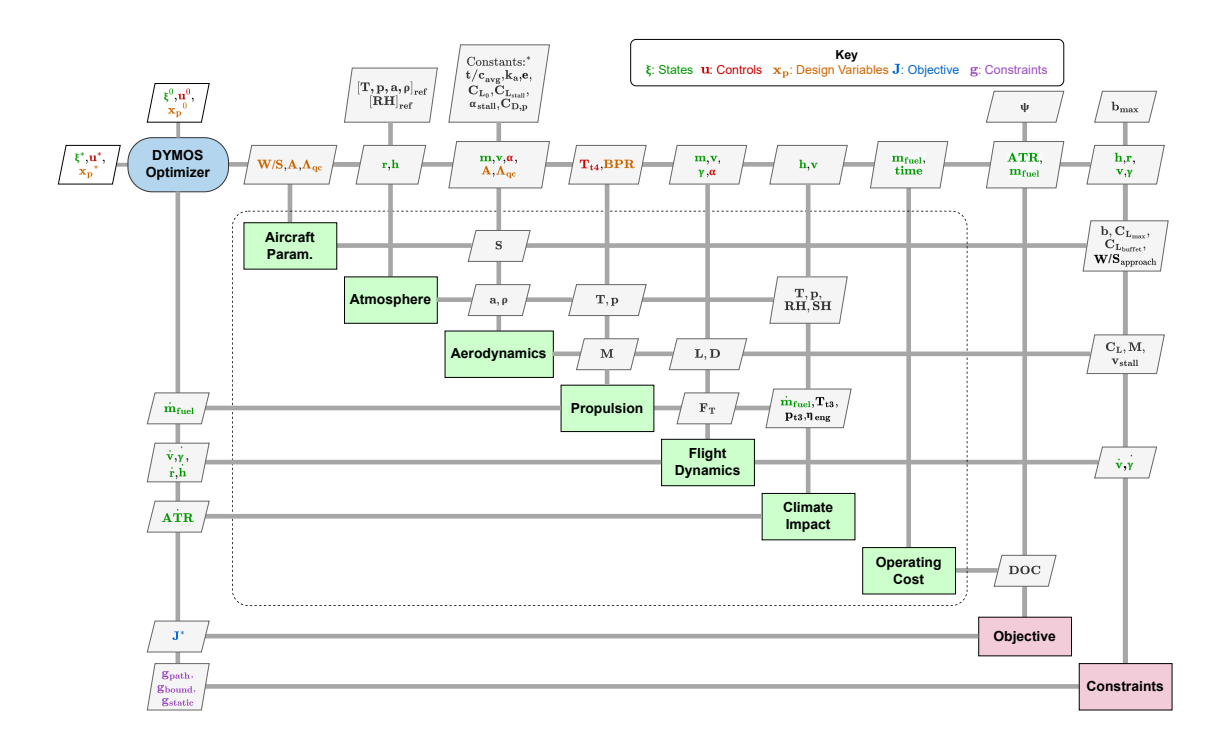


Figure 1: eXtended Design Structure Matrix (XDSM) of the full optimization problem

# 3. Modelling

# 3.1 Atmosphere

The atmospheric model defines properties of the environment that affect aerodynamics, propulsion, emissions, and climate impact. The 1976 U.S. Standard Atmosphere<sup>5</sup> is used for reference data. This is complemented with experimental humidity data taken from Held.<sup>14</sup> Humidity is varied with distance along the mission profile to create a representative atmosphere model containing regions where contrails will form and others where they will not. Humidity is used to estimate NO<sub>x</sub> emission rates, while contrails are formed based on both humidity and temperature.

The humidity profile is chosen to roughly match the percentage of flight distance in which contrails are expected to persist in a typical medium-range, mid-latitude flight, according to Burkhardt and Kärcher.<sup>2</sup> As an outcome of this choice, the resulting climate impact contribution of contrails for a cost-optimal flight is comparable to that presented by Lee et al.,  $^1$  although it is noted that they measure climate impact in ERF and not ATR<sub>100</sub>.

# 3.2 Aerodynamics

The aerodynamic model determines the lift and drag curves to be used during the flight dynamic simulation. The lift polar (Equation 5) is assumed linear between a zero-incidence lift coefficient  $C_{L_0} = 0.3$ , and a maximum lift coefficient  $C_{\max} = 1.5$  at an angle of attack  $\alpha_{\max} = 7$  deg, as inferred from Airbus A320 lift curve data from Sun et al. aerodynamics model from Falck et al. are aerodynamics model from Falck et al.

$$C_L = C_{L_0} + \frac{\alpha}{\alpha_{\text{max}}} \left( C_{L_{\text{max}}} - C_{L_0} \right)$$
 (5)

The drag polar is composed of zero-lift drag  $C_{D_0}$ , lift-induced drag  $C_{D_1}$ , and wave drag  $C_{D_w}$  (Equation 6). The zero-lift drag includes parasitic drag  $C_{D_{0P}}$ , size-dependent ( $\Delta C_{D_{ED}}$ ) and size-independent excrescence ( $\Delta C_{D_{EI}}$ ) drag. The parasitic drag coefficient is assumed to be 0.0175, based on the low Mach number performance curves of an Airbus A320 by Sun et al.<sup>15</sup> Size-dependent excrescence drag is assumed to add 1.5%. Size-independent excrescence drag is modelled as 0.035/S. The lift-induced drag coefficient has a quadratic relation to the lift coefficient, which depends on the aspect ratio. The Oswald factor e is assumed to be 0.8. The wave drag coefficient  $C_{D_w}$  is estimated by the extended Korn equation, while the drag-divergence Mach number  $M_{dd}$  is given by Equation 7.<sup>16</sup>

$$C_D = C_{D_{0P}} + \Delta C_{D_{ED}} + \Delta C_{D_{EI}} + \frac{C_L^2}{\pi A e} + 20 \left( M - M_{dd} + \sqrt[3]{\frac{0.1}{80}} \right)^4$$
 (6)

Drag divergence depends on the quarter-chord sweep angle  $\Lambda_{\rm qc}$ , while the wing thickness-to-chord ratio has been assumed as  $t/c_{\rm avg}=0.12$ , and the airfoil technology factor as  $k_{\rm a}=0.935$ . The local critical lift coefficient  $C_{L_{\rm crit}}$  describes the lift coefficient of the most critical wing section, which we assume is higher than the wing lift coefficient. To characterize this parameter, it is assumed that the overall wing lift coefficient  $C_{L_{\rm wing}}$  is 10% lower than  $C_{L_{\rm crit}}$ , and 3% higher than that of the complete aircraft, therefore  $C_{L_{\rm crit}}=C_L\cdot 1.03/0.9$ .

$$M_{\rm dd} = \frac{k_{\rm a}}{\cos \Lambda_{\rm qc}} - \frac{t/c_{\rm avg}}{\cos^2 \Lambda_{\rm qc}} - \frac{C_{L_{\rm crit}}}{10\cos^3 \Lambda_{\rm qc}}$$
(7)

# 3.3 Propulsion

Thrust is provided by two high-bypass, twin-spool turbofan engines closely matched to the state-of-the-art CFM Leap-1A engine. An analytical surrogate model is developed on the basis of the propulsion model used by Proesmans and Vos.<sup>6</sup> Their technique employed methods from Mattingly et al.<sup>18</sup> to parametrically determine design-point thermodynamic cycle conditions at the cruise flight phase (Table 4), and then perform an off-design analysis to determine the thrust T, fuel flow  $m_f$ , temperature  $T_{T3}$  and pressure  $p_{T3}$  before the combustion chamber, and overall engine efficiency  $\eta_{eng}$  at varied flight conditions. In this work, a simplified algebraic thrust model is developed, which simplifies the calculations and improves the stability of the optimization. This surrogate model is designed to closely match the behavior of the model by Proesmans and Vos,<sup>6</sup> for the aforementioned outputs. This model estimates the outputs based on the variation of the input variables from their design values. These inputs include the control variable  $T_{T4}$ , the atmospheric temperature and pressure, and the flight Mach number. A verification plot is provided in Figure 4.

Table 4: Design parameters of the reference engine. PE = Polytropic Efficiency, LP = Low Pressure, HP = High Pressure

(a) Design requirements at cruise

Parameter	Value	Unit
Total Air Mass Flow	173	kg/s
Design Turbine Entry Temperature	1480	K
Static Temperature	216.65	K
Static Pressure	22 632	Pa
Fan Pressure Ratio	1.4	-
LPC Pressure Ratio	1.4	-
HPC Pressure Ratio	27.0	-

(b) Design assumptions<sup>6</sup>

Parameter	Value
Fan PE	0.915
Compressor PE (LP & HP)	0.9
Turbine PE (LP & HP)	0.93
Inlet Pressure Ratio	0.98
Combustor Pressure Ratio	0.96

# 3.4 Flight Dynamics

The equations of motion for symmetric flight in a vertical plane are used to simulate the dynamic evolution of the aircraft during the mission. These consist of two dynamic states (airspeed V and flight path angle  $\gamma$ ) and two kinematic states (altitude h and horizontal distance r). Their rates of change are expressed through Equations 8, where the thrust force  $F_T$  is assumed to be aligned with the aircraft longitudinal body axis. The loss of aircraft weight is solely due to fuel burn, which is determined by the propulsion model

$$\dot{V} = \frac{F_T \cos \alpha - D}{m} - g \sin \gamma \qquad \dot{\gamma} = \frac{F_T \sin \alpha + L}{mV} - \frac{g}{V} \cos \gamma \qquad \dot{h} = V \sin \gamma \qquad \dot{r} = V \cos \gamma \qquad \dot{m} = -\dot{m}_f \qquad (8)$$

#### 3.5 Emissions and Climate

Climate impact is determined from aircraft emissions and local atmospheric conditions, and quantified in terms of ATR<sub>100</sub>. Emission species considered are carbon dioxide (CO<sub>2</sub>), nitrogen oxides (NO<sub>x</sub>), water vapour (H<sub>2</sub>O), sulphates (SO<sub>4</sub>), and soot. NO<sub>x</sub> is not a greenhouse gas, but leads to long-term depletion of methane (NO<sub>x</sub>-CH<sub>4</sub>) and ozone (NO<sub>x</sub>-O<sub>3L</sub>), and short-term production of ozone (NO<sub>x</sub>-O<sub>3S</sub>). Emission rates  $\dot{E}_i$  are determined, for every species, by multiplying the Emission Index (EI), which indicates the mass of pollutant produced per kilogram of fuel burned, by the instantaneous fuel flow, as shown in Equation 9. Table 5 shows the EIs, assumed constant, for the different species.

$$\dot{E}_i = \mathrm{EI}_i \cdot \dot{m}_\mathrm{f} \tag{9}$$

Table 5: Selected Emission Indices (EIs) of different chemical species<sup>3</sup>

	CO <sub>2</sub>	H <sub>2</sub> O	SO <sub>4</sub>	Soot
Emission Index EI (kg/kg)	3.16	1.26	2.0×10 <sup>-4</sup>	4.0×10 <sup>-4</sup>

 $NO_x$  emissions depend on engine operating conditions and atmospheric specific humidity  $H_0$ , which is captured in Equation 10.<sup>19</sup> The engine parameters are the total pressure  $p_{T3}$  and temperature  $T_{T3}$  at the combustor inlet.

$$EI_{NO_x} = 0.0986 \cdot \left(\frac{p_{T3}}{101325}\right)^{0.4} \cdot \exp\left(\frac{T_{T3}}{194.4} - \frac{H_0}{53.2}\right)$$
 (10)

The ATR<sub>H</sub> is the global near-surface temperature response averaged over a lifetime H, as initially proposed by Dallara et al.<sup>3</sup> and shown in Figure 2. The radiative forcing and temperature response due to aircraft fleet emissions are calculated on the basis a sustained period of operation, which is assumed proportional to the fleet size. In this work, the fleet is assumed to grow to 17 million flights per year over a 30-year production window. With an expected aircraft lifetime of 35 years, the fleet will be fully retired after 65 years. The ATR lifetime H is taken as 100 years, hence the symbol ATR<sub>100</sub>. The fleet size is included in radiative forcing calculations as the function  $flt(\tau)$ .

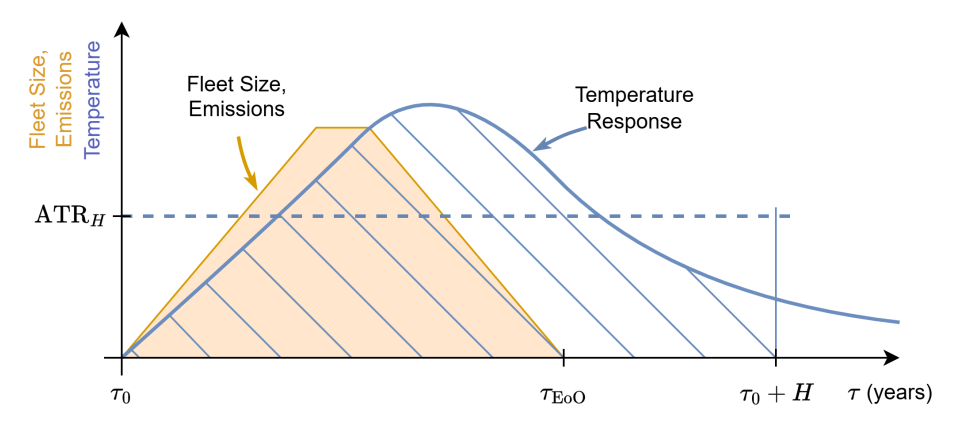


Figure 2: Illustration of the ATR due to aircraft fleet emissions, over a time period H from entry into service  $t_0$  until end of operations  $t_{EoO}$ .

The climate impact at each node of the mission profile is considered by modelling the rate of change of ATR, as shown in Equation 11.

$$A\dot{\Gamma}R_H = \frac{1}{H_{ATR}} \int_0^H \Delta \dot{T}(\tau) d\tau \tag{11}$$

In the integral,  $\Delta T(\tau)$  is the global near-surface temperature response in year  $\tau$  due to the evolution of radiative forcing due to aircraft emissions. Its rate of change is given by Equation 12, which convolves the radiative forcing rate  $RF^*(\tau)$  with a response function  $G_T(\tau - \tau')$ , which depends on the type of emission.

$$\Delta \dot{T}(\tau) = \int_{\tau_0}^{\tau} G_T(\tau - \tau') \, \dot{R} \dot{F}^*(\tau') d\tau' \tag{12}$$

The rate of change of radiative forcing  $\dot{R}\dot{F}^*(\tau)$  is given by Equation 13, which sums the contributions of all species, each weighted by a climate efficacy factor  $f_i$ .<sup>20,21</sup>

$$\dot{R}\dot{F}^*(\tau) = \sum_{i}^{\text{all species}} \left( f_i \frac{\dot{R}\dot{F}_i(\tau)}{RF_{2\times CO_2}} \right)$$
 (13)

The calculation procedure is essentially the same as the one presented by Dallara et al.<sup>3</sup> The difference lies in the temperature response (Equation 12) and radiative forcing effects (Equation 13) being determined as rate per second of flight time. These calculations are then based on emission rates, rather than cumulative emissions. For the radiative forcing due to contrails, this translates to a dependency on aircraft airspeed, rather than total distance. A similar method was used by Lührs et al.<sup>7</sup>

#### 3.5.1 Carbon Dioxide

As carbon dioxide is a long-lived greenhouse gas, its emission is convoluted with a response function  $G_{\chi_{\text{CO}_2}}(\tau)$ , which describes the relatively slow decay of the perturbation over time (Equation 14).  $G_{\chi_{\text{CO}_2}}$  is taken from Sausen and Schumann<sup>22</sup> and verified by Proesmans and Vos.<sup>6</sup> The fleet size over time is included as  $flt(\tau)$ .

$$\Delta \dot{\chi}_{\rm CO_2}(\tau) = \int_{\tau_0}^{\tau} G_{\chi_{\rm CO_2}}(\tau - \tau') \cdot flt(\tau) \cdot \dot{E}_{\rm CO_2}(\tau') d\tau'$$
 (14)

The radiative forcing rate of  $CO_2$  in Equation 15 depends on the perturbation rate  $\Delta \dot{\chi}_{CO_2}(\tau)$  and background concentration  $\chi_{CO_2,0}$ , assumed to be 380 ppmv.

$$\dot{RF}_{CO_2}^*(\tau) = \frac{1}{\ln 2} \cdot \ln \left( \frac{\chi_{CO_2,0} + \Delta \dot{\chi}_{CO_2}(\tau)}{\chi_{CO_2,0}} \right)$$
(15)

# 3.5.2 Nitrogen Oxides

Similar to the approach for CO<sub>2</sub>, the NO<sub>x</sub>-induced methane and long-term ozone effects are modelled with a perturbation response function  $G_i(\tau)$  as laid out by Dallara et al.<sup>3</sup> The resulting radiative forcing rate is modelled as follows:

$$\dot{RF}_{i}(\tau,h) = s_{i}(h) \int_{\tau_{0}}^{\tau} G_{i}(\tau - \tau') \cdot flt(\tau) \cdot \dot{E}_{NO_{x}}(\tau') d\tau'$$
(16)

Nitrogen oxides do not diffuse quickly through the atmosphere like  $CO_2$ , and the climate response to methane and ozone differs with altitude. This is accounted for by the forcing function  $s_i(h)$ , obtained from Dallara et al.<sup>3</sup> A radiative forcing sensitivity  $RF_{ref}/E_{ref}$  accounts for the strength of the greenhouse effect caused by the emission species, and is measured in  $W/m^2/kg$ . For  $NO_x$ -induced methane and long-term ozone, this factor is included in the response function  $G_i(\tau)$ . Short-term ozone is modelled more simply and includes radiative forcing sensitivity directly:

$$\dot{RF}_{NO_x-O_{3S}}(\tau,h) = s_{NO_x-O_{3S}}(h) \cdot \left(\frac{RF_{ref}}{E_{ref}}\right)_{NO_x-O_{3S}} \cdot flt(\tau) \cdot \dot{E}_{NO_x}(\tau)$$
(17)

#### 3.5.3 Contrails

In the current setup, we only model the climate impact of persistent contrails. Contrail persistence is evaluated based on three conditions. First, the Schmidt-Applemann Criterion (SAC) is used to determine whether the engine exhaust reaches saturation with respect to water, as it mixes with ambient air.<sup>23</sup> Second, the condensation must freeze, which occurs around -38 °C at typical cruise altitudes. Finally, contrails persist only if the mixed and cooled exhaust has a partial vapour pressure above the saturation point with respect to ice, which is determined using a formulation by Sonntag.<sup>24</sup>

The formation criteria result in a binary nature of contrail persistence. This is a strong assumption to make, considering atmospheric mixing effects and uncertainties in the atmospheric model. Moreover, it creates a strong and unpredictable discontinuity, which is undesired for the numerical convergence of the OCP. To avoid this, a climate impact "gradient" has been introduced by weighting each of the three persistence criteria mentioned above with a hyperbolic tangent function. These smoothen the verification of the criterion on the basis of the proximity to satisfaction of that condition, and therefore enable the optimizer to make decisions based on continuous gradients.

If conditions are right for contrails to persist at any point along the mission profile, the following radiative forcing rate is applied at the corresponding nodes.

$$\dot{RF}_{con}(\tau, h) = s_{con}(h) \cdot \left(\frac{RF_{ref}}{L_{ref}}\right)_{con} \cdot flt(\tau) \cdot V \times 10^{-3}$$
(18)

Like methane and ozone, the radiative forcing impact of contrails is dependent on the altitude that they form. The forcing function  $s_{con}(h)$  accounts for this variation, and is obtained from Dallara et al.<sup>3</sup> The radiative forcing sensitivity for contrails is defined per unit length (RF<sub>ref</sub>/ $L_{ref}$ ) and is taken as  $1.82 \times 10^{-12}$  W/m<sup>2</sup>/km.<sup>1</sup> Therefore, the calculation of the RF rate in Equation 18 includes the flight velocity converted to km/s.

A Contrail Persistence Region (CPR) is defined here as a portion of the atmosphere which satisfies the conditions for contrails to persist. In this work, a static 2-dimensional atmospheric temperature and humidity model is generated to create random but realistic CPRs, thereby testing the ability of the mission profile optimizer to avoid such regions. The baseline atmosphere is illustrated in Figure 3 by blue shading that represents the contrail persistence weighting. This indicates the relative radiative forcing that would result from a contrail formed at that location. The shading is based on the assumption that an aircraft flying in the region burns kerosene and is operating at 30% overall efficiency.

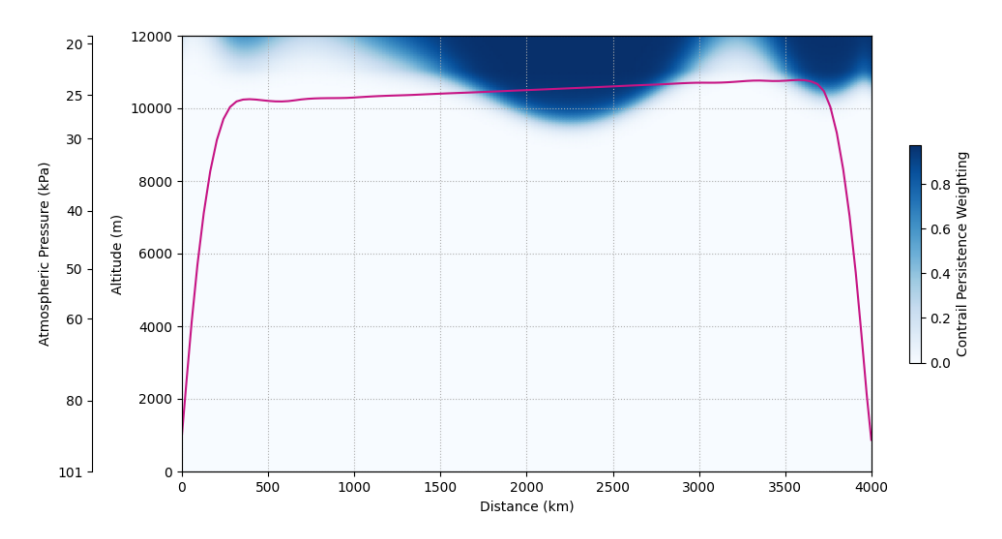


Figure 3: The baseline atmospheric case illustrated by the contrail persistence weighting at each point in a two-dimensional space. A cost-optimal flight profile is overlaid.

# 3.5.4 Water Vapour, Sulphates & Soot

Similar to short-term ozone, water vapour, sulphates and soot impact global radiative forcing in the short term. Altitude dependency is not considered. Their radiative forcing rates are given by the following Equation 19.

$$\dot{RF}_{i}(\tau) = \left(\frac{RF_{ref}}{E_{ref}}\right)_{i} \cdot flt(\tau) \cdot \dot{E}_{i}(\tau)$$
(19)

# 3.6 Direct Operating Costs

Direct operating costs are composed of crew salaries, time-dependent maintenance costs and fuel costs. Crew rates for narrowbody aircraft are assumed at \$14.5/min based on Airbus's cost indexing guide<sup>25</sup> and accounting for inflation. Time-dependent maintenance costs are assumed at \$7/min.<sup>25</sup> A fuel price of 0.70 \$/kg is taken in September 2024 from the International Air Transport Association (IATA)<sup>1</sup>.

# 4. Model Verification

The propulsion model has been verified against the model of Proesmans and Vos.<sup>6</sup> Figure 4 compares the fuel flow, thrust, temperature and pressure before the combustor, and overall efficiency, for a given history of the  $T_{\rm T4}$  input.

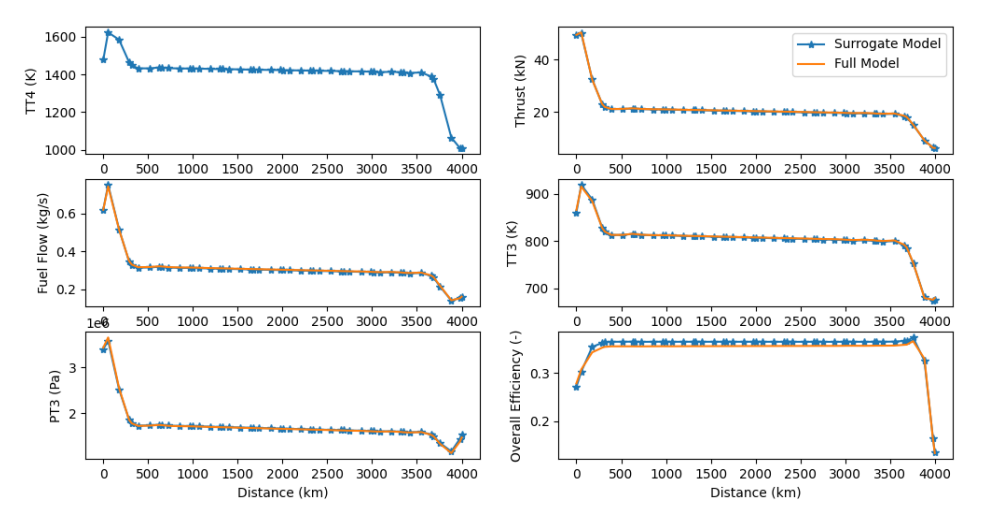


Figure 4: Verification of the surrogate propulsion model for the reference cost-optimal flight path.

The climate model was verified against the results of Proesmans and Vos<sup>6</sup> and Lee et al.<sup>1</sup> The ATR measure is dependent on the fleet definition as described in Section 3.5, which matches the one defined by Proesmans and Vos.<sup>6</sup> The baseline cost-optimal flight over a range of  $4000 \,\mathrm{km}$  results in  $\mathrm{ATR}_{100} = 17.6 \,\mathrm{mK}$ . When compared to the  $12 \,\mathrm{mK}$  to  $27 \,\mathrm{mK}$  spectrum found by Proesmans and Vos,<sup>6</sup> this is considered a satisfactory correlation, given the broad assumptions made. The contribution of each species to the total  $\mathrm{ATR}_{100}$  is shown in the breakdown of Figure 5. It correlates with well-known climate impact analyses of aviation on the global greenhouse effect.<sup>1</sup> It is noted however, that the metrics used in the present and reference studies are different: Lee et al. report climate response in  $\mathrm{ERF}^1$  rather than  $\mathrm{ATR}_{100}$ .

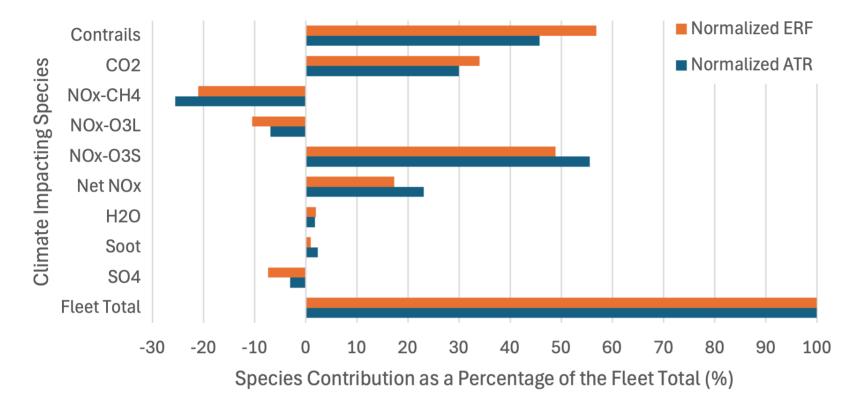


Figure 5: Normalized breakdown of ATR<sub>100</sub> contributions to the total fleet ATR for a baseline cost-optimal flight over a 4000 km range, in comparison to ERF results from Lee et al.<sup>1</sup>

<sup>&</sup>lt;sup>1</sup>https://www.iata.org/en/publications/economics/fuel-monitor/

# 5. Results

# 5.1 Baseline aircraft design

For this first case, the aircraft design is fixed at the narrow-body baseline (Table 3), with a payload mass of  $16\,000\,\mathrm{kg}$ . The mission profile is optimized for different cost-weighted objectives, over a range of  $4000\,\mathrm{km}$ . Figure 6 compares the controls ( $\alpha$  and  $T_{\mathrm{T4}}$ ), states, and relevant flight parameters for the DOC-optimal and ATR-optimal mission profiles.

The ATR-optimal mission maintains an overall lower cruise speed and a larger margin to the drag divergence velocity. This corresponds to a lower Mach number and wave drag. The climate-optimal profile most notably presents a localized drop in altitude and speed from about 1500 km to 3000 km. This avoids a CPR and reduces the climate impact of the mission by 54.8%. Table 6 provides a comparison of indicative values for the objectives of DOC, ATR, and fuel. This demonstrates the potential for climate impact reduction by avoiding CPRs, as well as the associated increase in cost and time.

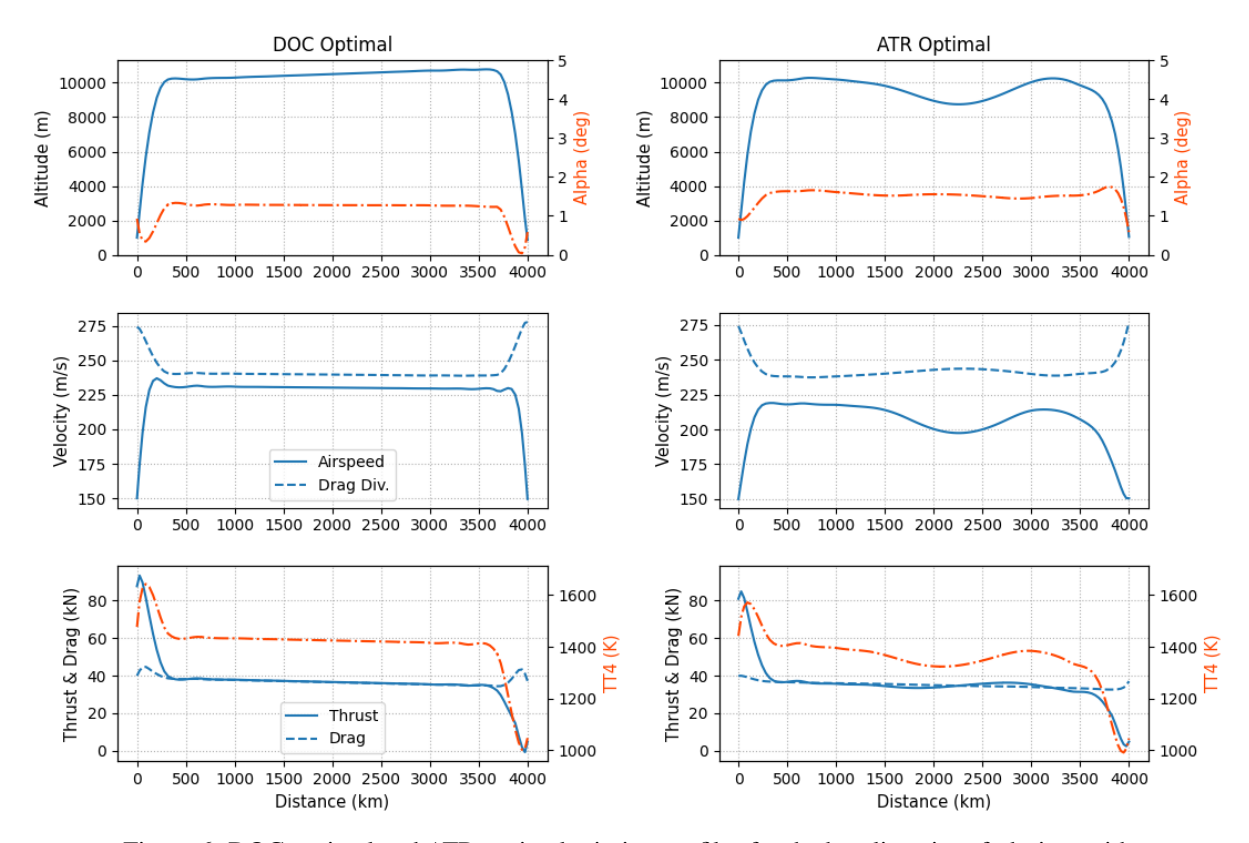


Figure 6: DOC-optimal and ATR-optimal mission profiles for the baseline aircraft design, with given 4000 km range and 16 000 kg payload mass.

Table 6: Path performance comparison for DOC-optimal and ATR-optimal missions

(a) Over a single flight

(b) Over the fleet lifespan

	DOC-optimal	ATR-optimal		DOC-optimal	ATR-optimal
Flight duration	4 hrs 53 min	5 hrs 25 min	DOC	$7.93 \times 10^{12}$ \$	$8.29 \times 10^{12}$ \$
Cruise Mach number	0.774	$0.730^{a}$	$ATR_{100}$	$17.6\mathrm{mK}$	$7.96\mathrm{mK}$
Avg. <sup>b</sup> cruise T <sub>T4</sub>	1430 K	1360 K	Fuel	$5.74 \times 10^{12} \mathrm{kg}$	$5.65 \times 10^{12} \mathrm{kg}$

<sup>&</sup>lt;sup>a</sup>Cruise flight is considered outside of contrail-affected regions, where the Mach number is constant and the flight path is not diverted below a CPR (800 km). <sup>b</sup>From 500 km to 3500 km.

The climate temperature response is composed of short- and long-term effects, and the effects of the different emission species peak at different times. Figure 7 illustrates the time history of Earth's surface temperature response due to each

emission species, over a time span of over 100 years, for DOC-optimal and ATR-optimal mission profiles. The subfigures demonstrate the significant reduction in the climate response that can be achieved by minimizing the formation of contrails, but also that the effects of the latter are relatively short-lived. On the other hand, CO<sub>2</sub> is a longer-impacting agent with effects lasting decades after fleet retirement. These insights may be relevant when investigating hydrogen or sustainable aviation fuels with innovative emissions compositions.

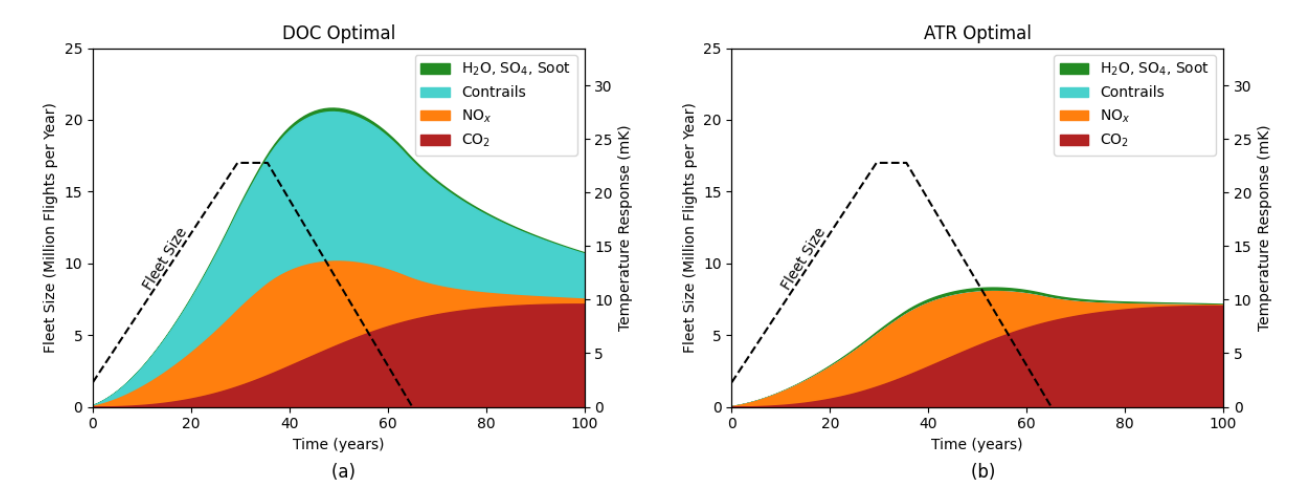


Figure 7: Net temperature response per emission species, over a 100-year time span, for DOC-optimal and ATR-optimal mission profiles.

# 5.2 Mission Profile and Aircraft Design Co-optimization

For this second case, the wing plan form is co-optimized together with the mission profile, again for different cost weightings. Figure 8 summarizes the profile and design results. As expected, high cost weightings result in mission profiles passing through or close to the CPR, preferring cost optimality over climate impact. As the cost weighting is reduced, the cruise altitude decreases, together with the sweep angle of the wing.

However, even with relatively high cost weightings (up to 0.98), the CPR is mostly avoided, hinting at the fact that contrail avoidance is a cost-effective strategy to reduce climate impact. Interestingly, the mission profile optimized for  $\psi = 0.995$  results in an oscillating profile which only crosses the lower part of the CPR, in between 2000 km to 2500 km. This behaviour is the result of modelling artefacts, and is not recommended for operational practice.

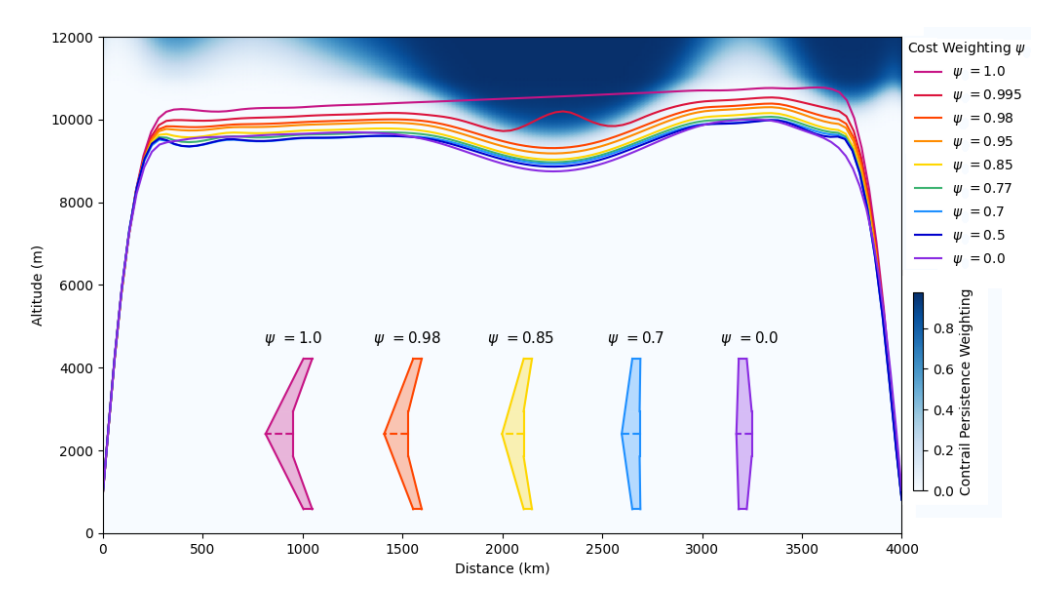


Figure 8: Co-optimized 4000 km trajectories and aircraft design with varied cost weighting. Climate-optimal solutions avoid the CPRs indicated in blue.

Figure 9 displays the wing sweep and aspect ratio relative to the cruise Mach number, in correlation with the corresponding value of the cost weighting parameter  $\psi$ . For consistency, the cruise Mach number was taken at a steady-state, high-altitude point in the flight which did not fall within a CPR (in this case, at a distance of 800 km). Lower design Mach numbers correspond to lower optimal sweep angles, as the impact of wave drag on mission performance becomes less prominent. Wings with lower sweep angles achieve a higher maximum lift coefficient, in the current design setup, and therefore result in a higher wing loading and smaller area. In all cases, the wingspan limit of 36 m is reached. In this condition, with the MTOM being fixed, wing loading and aspect ratio become proportional according to Equation 20. A higher wing loading results therefore in a higher wing aspect ratio. For cost weightings  $\psi < 0.65$ , the wing geometry remains fixed with no sweep angle.

$$AR = \frac{b^2}{S} \Rightarrow AR = \frac{b_{\text{max}}^2}{\text{MTOM} \cdot g} (W/S)$$
 (20)

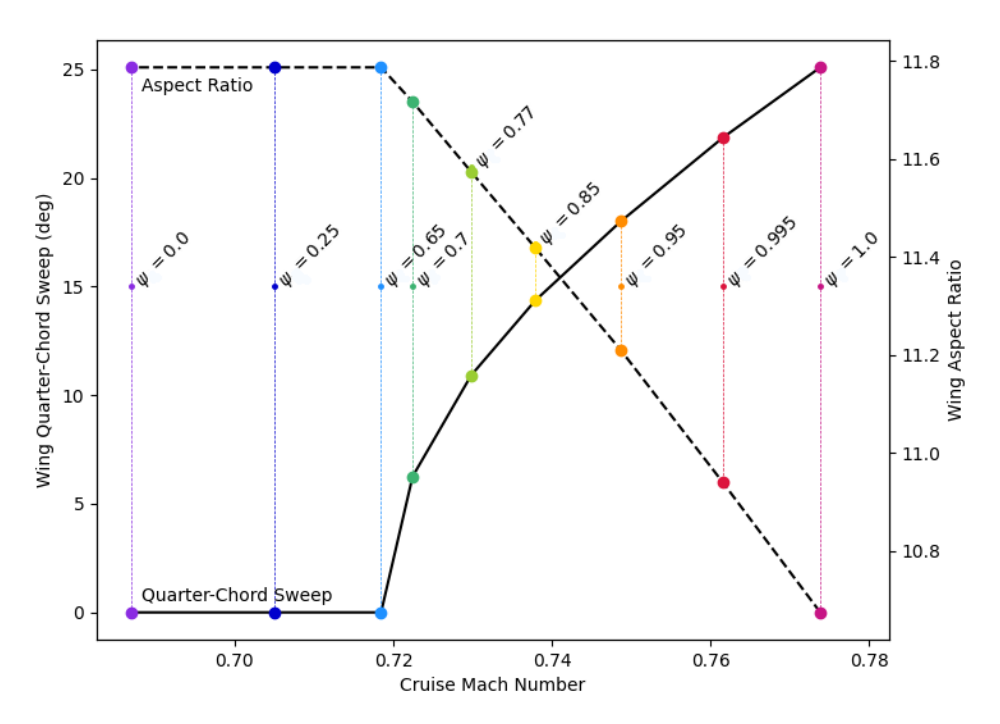


Figure 9: Relation between optimal cruise Mach number and selected wing quarter-chord sweep angle and aspect ratio for varying cost weighting factors  $\psi$ .

Figure 10 illustrates the trade-off between DOC and ATR for mission profiles optimized with different cost weighting indices. Values are normalized with respect to the cost-optimal trajectory obtained with the baseline aircraft design, indicated by Point A. The benefit of a combined DOC-ATR objective is demonstrated by the effective trade-off between DOC and ATR for cost weightings between 0.5 and 0.98, visible in all reported cases. For the baseline aircraft design, a cost weighting of 0.85 provides a 49% reduction in ATR with only 0.42% increase in DOC with respect to the cost-optimal solution (Point A). In this case, flight time slightly decreases (-0.21%), but fuel burn increases by 1.0%.

A significant improvement in DOC is obtained by co-optimizing the wing planform and mission profile for minimum cost, illustrated by Point B. The optimal mission profiles achievable with this cost-optimal wing planform, compared to the baseline wing planform, for different values of the cost weighting index  $\psi$ , consistently result in about 0.5% decrease in DOC and 1.0% decrease in ATR. Similarly to the above, optimizing the mission profile for a cost weighted objective of 0.85 (Point C) results in an ATR reduction of 49% and DOC increase of 0.42% compared to the cost-optimal case (Point B).

When the aircraft design is co-optimized with the mission profile for all values of the cost weighting  $\psi$ , the trade-off curve shifts down and to the left in Figure 10, demonstrating an improvement in both DOC and ATR. Compared to the cost-optimal aircraft design, the case of  $\psi=0.85$  (Point D) achieves an ATR reduction of 56% and an increase in DOC of just 0.32%. This is an improvement in terms of both DOC and ATR, compared to the cost-optimal aircraft design, indicating the effectiveness of the co-optimization. Flight time increases by 3.5%, equating to just over 10 minutes for the approximate five-hour flight. The co-optimized wing planform (corresponding to  $\psi=0.85$ ) features a sweep angle of 14.4 deg and an aspect ratio of 11.4.

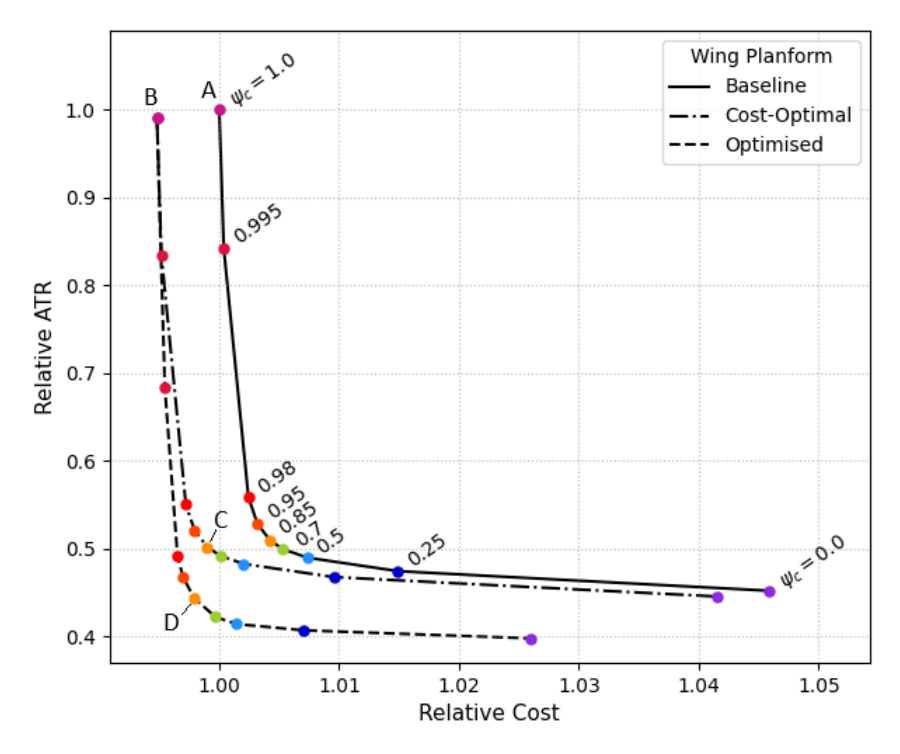


Figure 10: Trade-off curves of DOC and ATR for fixed baseline and cost-optimal aircraft designs, and for aircraft design co-optimized with the mission profile.

An improvement is seen when comparing the above case with the ATR-optimal aircraft design flying a cruise-climb mission profile studied by Proesmans and Vos.<sup>6</sup> In the latter case, the DOC increased by approximately 1.8% for a 50% reduction in ATR with respect to the baseline design – a higher cost compromise than the one obtained in this work. The improvement in this work is attributed to the mission profile optimization allowing a large portion of the flight to remain at a cost-effective altitude, and only descending to avoid climate-sensitive regions. Additionally, the DOC estimation method employed in this research differs from the one used by Proesmans and Vos.<sup>6</sup>

# 6. Conclusions

The climate impact of aviation can be reduced in a cost-effective way through global path performance optimization, mainly targeted at contrail avoidance. Simultaneous co-optimization of aircraft design and mission profile is beneficial in terms of both DOC and ATR, with little to no compromise. For cost weightings up to 0.98, optimal mission profiles almost entirely avoid contrail persistence. Only at very high-cost weightings of 0.995 and above, optimized mission profiles pass through contrail persistence regions, compromising climate impact to reduce operating costs.

An interesting trade-off is obtained for mission profiles optimized for an objective with a cost weighting  $\psi = 0.85$ . With a fixed aircraft design and optimized mission profile, the ATR is reduced by 49% and DOC is increased by just 0.42% with respect to the cost-optimal mission profile. This is the case if the aircraft design is fixed either at the baseline or the cost-optimal ( $\psi = 1$ ) case.

When the aircraft design and mission profile are co-optimized specifically for the objective  $\psi=0.85$ , the ATR is reduced by a further 7% and the DOC decrease by 0.10% compared to the same objective with a fixed cost-optimal aircraft design. Between the two single-objective cases ( $\psi=1$  and  $\psi=0$ .), the mean cruise Mach number drops from 0.770 to 0.737, while mean cruise altitude drops from 9930m to 9650m. This indicates that, on average, slower and lower flight can help to avoid contrails for mid-latitude routes.

For the co-optimized case, flight time increases by 3.5%, or 10 minutes over the 4000 km range compared to the baseline. The optimized aircraft has a quarter-chord wing sweep of 14.4 deg and an aspect ratio of 11.4, as compared to baseline values of 25 deg and 10.5 respectively.

Comparing DOC-optimal and ATR-optimal trajectories, most of the climate impact reduction is attributed to the shorter-term impacts from contrails and  $NO_x$ , whereas longer-term impacts from  $CO_2$  decrease by only 1.6%. ATR<sub>100</sub> mitigation through contrail avoidance may be deemed not as valuable as the mitigation obtained through minimization of carbon dioxide emissions, which have longer-term impact. However, results for minimum-fuel (and

therefore minimum  $CO_2$ ) mission profiles (not reported for brevity) show reductions in  $CO_2$  emissions by only a further 1.2% with respect to ATR-optimal ones. This indicates that methods and technologies other than aircraft design and profile optimization will be required for larger carbon impact reductions.

While the impacts of nitrogen oxides are not included in the ATR objective, it appears that the loss in climate optimality due to this assumption is not large. Future work should quantify the impact of the assumptions made about the shape of the contrail persistence region on the DOC-ATR trade-off curve. Also, the optimization study could be extended to allow for variable maximum take-off mass.

# 7. Acknowledgments

This work is based on the Master thesis research by Nicholas Lambrecht.

# References

- [1] D. S. Lee, D. W. Fahey, A. Skowron, M. R. Allen, U. Burkhardt, Q. Chen, S. J. Doherty, S. Freeman, P. M. Forster, J. Fuglestvedt, A. Gettelman, R. R. De León, L. L. Lim, M. T. Lund, R. J. Millar, B. Owen, J. E. Penner, G. Pitari, M. J. Prather, R. Sausen, and L. J. Wilcox. The contribution of global aviation to anthropogenic climate forcing for 2000 to 2018. *Atmospheric Environment*, 244:117834, January 2021.
- [2] Ulrike Burkhardt and Bernd Kärcher. Global radiative forcing from contrail cirrus. *Nature Climate Change*, 1(1):54–58, April 2011. Publisher: Nature Publishing Group.
- [3] Emily Schwartz Dallara, Ilan M. Kroo, and Ian A. Waitz. Metric for Comparing Lifetime average Climate Impact of Aircraft. *AIAA Journal*, 49(8):1600–1613, August 2011.
- [4] Liam Megill. Analysis of Climate Metrics for Aviation. Master's thesis, Delft University of Technology, Delft, The Netherlands, 2022.
- [5] Robert Falck, Justin Gray, Kaushik Ponnapalli, and Ted Wright. dymos: A Python package for optimal control of multidisciplinary systems. *The Open Journal*, 6(59):2809, March 2021.
- [6] Pieter-Jan Proesmans and Roelof Vos. Airplane Design Optimization for Minimal Global Warming Impact. *Journal of Aircraft*, 59(5):1363–1381, 2022.
- [7] Benjamin Lührs, Malte Niklass, Christine Froemming, Volker Grewe, and Volker Gollnick. Cost-Benefit Assessment of 2D and 3D Climate And Weather Optimized Trajectories. In *16th AIAA Aviation Technology, Integration, and Operations Conference*, volume 16 of *AIAA AVIATION Forum*, June 2016.
- [8] Shugo Kaneko and Joaquim R. Martins. MDO Formulations for Simultaneous Design and Trajectory Optimization. In AIAA SCITECH 2024 Forum, January 2024.
- [9] Ahmed W.A. Hammad, David Rey, Amani Bu-Qammaz, Hanna Grzybowska, and Ali Akbarnezhad. Mathematical optimization in enhancing the sustainability of aircraft trajectory: A review. *International Journal of Sustainable Transportation*, 14(6):413–436, June 2020. Publisher: Taylor & Francis.
- [10] Anil V. Rao. Trajectory Optimization. Encyclopedia of Aerospace Engineering, 2010.
- [11] Divya Garg, Michael Patterson, William Hager, Anil Rao, David R. Benson, and Geoffrey T Huntington. An overview of three pseudospectral methods for the numerical solution of optimal control problems. October 2017.
- [12] Ed Obert. Aerodynamic Design of Transport Aircraft. IOS Press, 2009.
- [13] Andrew B. Lambe and Joaquim R. R. A. Martins. Extensions to the design structure matrix for the description of multidisciplinary design, analysis, and optimization processes. *Structural and Multidisciplinary Optimization*, 46(2):273–284, August 2012.
- [14] Isaac Held. Relative humidity in "cloud resolving" models Geophysical Fluid Dynamics Laboratory, 2012.
- [15] Junzi Sun, Jacco M. Hoekstra, and Joost Ellerbroek. Openap: An open-source aircraft performance model for air transportation studies and simulations. *Aerospace*, 7(8), 2020.

- [16] Gabriel Pinho Chiozzotto. *Improving aircraft conceptual design with methods for wing loads, aeroelasticity and mass estimation*. PhD thesis, Technische Universität Berlin, 2019.
- [17] Gabriel Pinho Chiozotto. *Improving Aircraft Conceptual Design with Methods for Wing Loads, Aeroelasticity and Mass Estimation*. Phd, Technischen UniversitĤt Berlin, Göttingen, 2017.
- [18] Jack D. Mattingly, William H. Heiser, and David T. Pratt. *Aircraft Engine Design, Second Edition*. American Institute of Aeronautics and Astronautics, Reston, Virginia, 2002.
- [19] Emily Schwartz Dallara. Aircraft Design for Reduced Climate Impact. PhD thesis, Stanford University, 2011.
- [20] Michael Ponater, Susanne Pechtl, Robert Sausen, Ulrich Schumann, and Gerhard Hüttig. Potential of the cryoplane technology to reduce aircraft climate impact: A state-of-the-art assessment. *Atmospheric Environment*, 40(36):6928–6944, November 2006.
- [21] Intergovernmental Panel on Climate Change. Climate Change 2007: The Physical Science Basis, Contribution of Working Group I to the Fourth Assessment Report of the Intergovernmental Panel on Climate Change. Technical Report Chapter 2, Cambridge University Press, Cambridge, England, U.K., 2007.
- [22] Robert Sausen and Ulrich Schumann. Estimates of the Climate Response to Aircraft CO2 and NOx Emissions Scenarios. *Climatic Change*, 44(1):27–58, January 2000.
- [23] H. Appleman. The formation of exhaust condensation trails by jet aircraft. *Bulletin of the American Meteorological Society*, 34(1):14–20, January 1953.
- [24] Dietrich Sonntag. Important new values of the physical constants of 1986, vapour pressure formulations based on the its-90, and psychrometer formulae. *Zeitschrift für Meteorologie*, 40(5):340–344, 1990.
- [25] Airbus. Getting to grips with the cost index. 1998.